# Controlled Liquid–Air Interfaces and Interfacial Polymer Micromembranes in Microfluidic Channels

Daming Cheng, Young-Joon Paul Choe, and Hongrui Jiang, *Member, IEEE*

***Abstract*—In this paper, we report on stable liquid–air interfaces and high-aspect-ratio polymer micromembranes with complex and controlled structures formed within microfluidic channels. Selective alkanethiol treatment on gold and copper surfaces is employed to create hydrophilic–hydrophobic boundaries between glass and these metal surfaces within microchannels. Robust liquid–air interfaces, featured with different 3-D structures, are formed at these boundaries. The process for creating these liquid–air interfaces is highly reproducible. Simulations are conducted to further study the liquid–air interfaces. The liquid–air interfaces are then utilized for interfacial polymerization. Two immiscible liquid phases containing the reagents react and generate polymer micromembranes within microfluidic channels. Formed following the hydrophilic–hydrophobic boundaries, these membranes have not only complex footprints on the substrates but also different configurations in the $z$-direction. Here, we demonstrate high-quality and complex 3-D nylon micromembranes fabricated in microchannels using this method. [2007-0294]**

***Index Terms*—Hydrophilic–hydrophobic boundary, interfacial polymerization, liquid–air interface, liquid–liquid interface, microfluidics, surface tension.**

## I. INTRODUCTION

STABLE and controlled microfluidic interfaces have potential applications in sensing and detecting chemical and biological agents [1], [2]. First, such interfaces within microfluidics can be liquid–air interfaces [3]. The liquid–air interfaces in microchannels have been utilized in, for instances, detecting airborne target agents [3], [4], sample acquisition for gas chromatography [5], measuring air pressure [6], and detecting droplets [7], [8]. Second, interfaces between two immiscible liquids are also been broadly studied. Such interfaces can also be utilized in sensing biological and chemical agents. For example, at the interfaces of an aqueous solution and a liquid crystal, which consists of anisotropic molecules, the arrangement or orientation of the molecules of the liquid crystal can be changed through interface chemical reaction, which can be used for sensing the presence of target agents in liquids [9]–[11]. On the other hand, physical walls or membranes at the interfaces also have applications in biological and chemical sensing. Such physical walls can be made of, for instance, polymers that can be specifically dissolved or compromised by certain agents [12], [13].

In microfluidic systems, where the channel structures have the dimensions ranging from tens to hundreds of micrometers, the capillary force and surface tension are dominant, compared to, for instance, the gravity [2], and can be exploited to create controlled multiphase interfaces in horizontal or vertical directions. The liquid–air interfaces can be created at hydrophilic–hydrophobic boundaries in microchannels because of the surface tension [14]. Coating with self-assembled monolayers (SAMs) of certain polymer molecules has been broadly used to change the wetting property of the surfaces in the microchannels [15]–[19] to create the hydrophilic–hydrophobic boundaries and, thus, to control the liquid–air or liquid–liquid interfaces [14], [20]. Laminar flow of the solution containing octadecyl trichlorosilane has been employed to divide a channel into hydrophobic and hydrophilic regions [2]. However, it is difficult to use this method to create complex shapes of hydrophilic–hydrophobic boundaries. Photocleavable SAM has also been applied to pattern the hydrophobic region into different shapes as designed [14], [18], [19], [21], [22]. However, the chemical process is relatively complicated.

Surface treatment on copper (Cu) and gold (Au) layers by coating with SAM of alkanethiols molecules makes the Au or Cu surface hydrophobic [23]–[25], while the alkanethiol SAM rarely forms on top of glass surface, thus forming a boundary between the areas with and without the SAM. In this paper, we harness the selective alkanethiol SAM formation on the metal layers (Cu and Au) to realize hydrophilic–hydrophobic boundaries. We recently reported preliminary results on such boundaries between alkanethiol-treated Cu patterns deposited on glass slides and glass surfaces [26]. Here, we extend this method to fabricate more complex liquid–air interfaces, such as straight-line, curved, interdigital, and twisted structures. The smallest feature size of the liquid–air interface structure is only limited by the surface tension. The whole process of this method takes only 3 h, and the interface generated shows high stability and reproducibility over multiple experiments. Simulations of the liquid–air interfaces are conducted. The interfaces of two immiscible liquid phases containing reagents are established for interfacial polymerization to form polymer membranes at the site of the interface. To demonstrate this fabrication method, thin nylon micromembranes with different 3-D structures that precisely follow the structures of the liquid–liquid interfaces are realized in microchannels.

---

Manuscript received December 10, 2007; revised March 19, 2008. First published June 20, 2008; last published August 1, 2008 (projected). This work was supported by the U.S. National Science Foundation under Grant ECCS 0622202. Subject Editor C. Mastrangelo.

D. Cheng is with the Materials Science Program, University of Wisconsin—Madison, Madison, WI 53706 USA.

Y.-J. P. Choe is with Northwestern University, Evanston, IL 60208 USA.

H. Jiang is with the Department of Electrical and Computer Engineering and the Materials Science Program, University of Wisconsin—Madison, Madison, WI 53706 USA (e-mail: hongrui@engr.wisc.edu).

Color versions of one or more of the figures in this paper are available online at http://ieeexplore.ieee.org.

Digital Object Identifier 10.1109/JMEMS.2008.926142

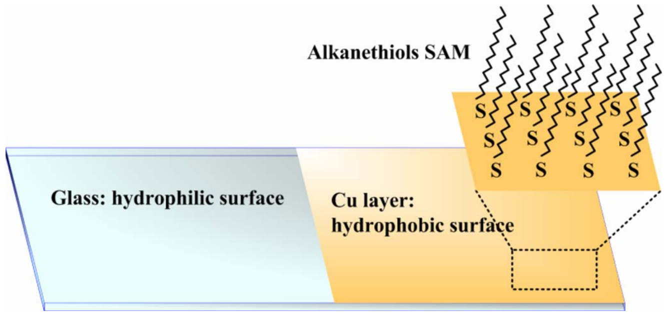

Fig. 1. Schematic illustration of the formation of a hydrophilic–hydrophobic boundary. The Cu coating on glass can be patterned by photolithography to create different boundary shapes. Monolayer of alkanethiols with the thickness of 10–25 Å [16] is formed on the Au or Cu surface. The hydrophilic–hydrophobic boundary forms at the edge between the metal and glass surfaces.

## II. Principle of Operation

### A. *Surface Treatment to Create Hydrophilic–Hydrophobic Boundaries*

When a hydrophilic–hydrophobic boundary is present on a surface, molecules of aqueous solutions will adhere to the hydrophilic side, where the surface free energy is large enough to prevent the aqueous solution from intruding into the hydrophobic side. Thus, a "pinned" liquid–air interface can be formed at such a boundary [1], [2].

SAM prepared by chemisorptions on a surface changes the free surface energy and can significantly increase the contact angle of aqueous solution on the surface [23], [27], [28]. By immersing the surface into a solution containing long-chain alkanethiolates, such as 1-Hexadecanethiol $[\mathrm{CH_3(CH_2)_{15}SH}]$, the alkanethiolate molecules can easily be absorbed onto the surface of Au, silver, and Cu to form a quasi-crystalline SAM, while the formation of SAM on a glass surface is much slower than on those metal surfaces. Therefore, the wetting property of water on glass and metal surfaces will significantly be differentiated; i.e., a hydrophilic–hydrophobic boundary is formed, as shown in Fig. 1. Using the absorbed SAM on top of a Cu or Au layer to obtain hydrophobic layers has the following advantages.

1) The boundaries between hydrophilic–hydrophobic areas can be defined by photopatterning. Complex shapes of multiphase interfaces can be realized.
2) The metal layers that define the hydrophobic areas can also serve as electrodes for electrical sensing in potential applications.

In this paper, sputtered Cu layers on microscope glass slides and commercially available Au-coated glass slides (TA134, EMF Corporation, Ithaca, NY, USA) are both used. The sputtered Cu layers are thin enough (300 Å) to be translucent, allowing for direct visualization under a microscope in its transmission mode during the experiments. Au has been broadly used in biomedical devices, because it has good oxidation resistance and biocompatibility [29]. In the following sections, devices fabricated with translucent Cu layers are used for observing the formation of the liquid–air interfaces and the polymerization of the nylon micromembranes, while the ones with Au layers are used to test the maximum pressure within the microchannels that could be sustained by the hydrophilic–hydrophobic boundaries. The hydrophilic–hydrophobic boundaries can be designed and patterned into different complex shapes. The channel pressures in these configurations are calculated in later sections. When the microchannel structures are constructed, the two glass slides with hydrophilic–hydrophobic boundaries can be aligned with a desired offset (translational or angular) between each other. The upper and lower edges of the liquid–air interface are pinned at the hydrophilic–hydrophobic boundaries at the top and bottom glass substrates, respectively. The interface then forms between the two edges in a plane defined by the shapes as well as the relative positions of the boundaries on the top and bottom hydrophobic Au or Cu layers.

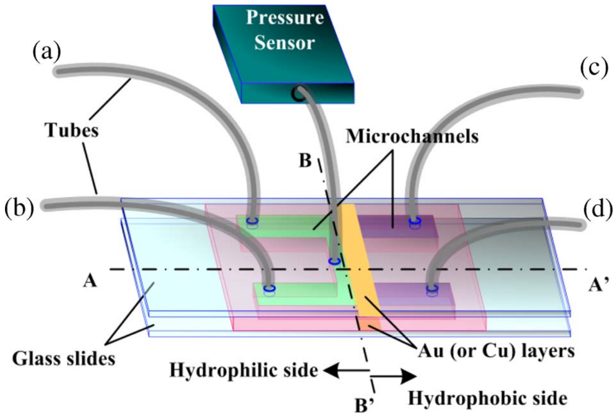

Fig. 2. Schematic illustration of a liquid–air interface formed with patterned Au or Cu layers on two glass slides. The interface can be defined into different configurations by patterning the Au or Cu layers into different shapes.

### B. *Theory on the Channel Pressure at the Hydrophilic–Hydrophobic Boundaries*

Fig. 2 shows the structure of a typical device in this paper. An "H"-shaped channel is constructed between two glass slides, which have patterned Au or Cu layers on the surfaces. The cross sections of the device are shown in Fig. 3. The left boundaries of the metal layer stripes are defined as the hydrophilic–hydrophobic boundary and are positioned in the middle of the center channel. The H-shaped channel is thus divided into a hydrophilic side and a hydrophobic side. In a typical experiment, the aqueous solution is introduced into the channel from inlet (a), as shown in Fig. 2. The liquid will fill the hydrophilic side of the channel, i.e., the left of $\mathrm{BB}'$, and later arrives at the outlet (b) of the hydrophilic side. The liquid–air interface is created in the center channel of the H-channel structure, along the hydrophilic–hydrophobic boundary.

As shown in Fig. 3, while being pumped into the channel, the aqueous solution behaves differently, in terms of the channel pressure and the shape of the liquid–air interface, in three stages. The pressure difference $\Delta P$ between the liquid $P$ and air $P_0$ can be determined by Young–Laplace equation [18], [30]

$$\Delta P = \gamma_{\mathrm{LG}} \left( \frac{1}{r} + \frac{1}{R} \right) \qquad (1)$$

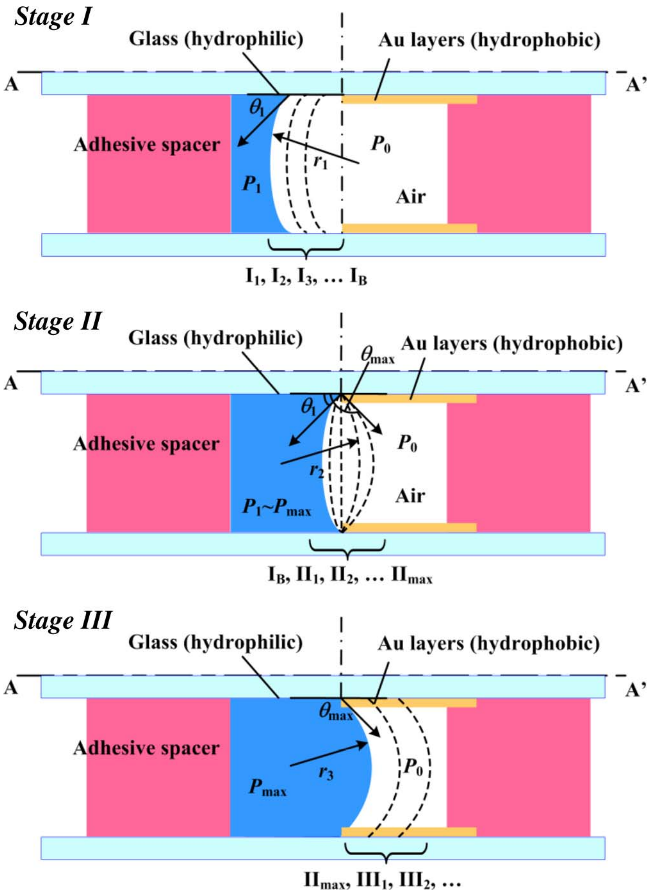

Fig. 3. Cross sections along AA$'$ in Fig. 2. When the front of the aqueous solution is still in the hydrophilic area, i.e., the left side of the hydrophilic–hydrophobic boundary, the liquid–air interface will maintain the same shape and move forward, shown as $\mathrm{I}_1, \mathrm{I}_2, \mathrm{I}_3, \ldots$ in Stage I, until arriving at the boundary. The pressure in the aqueous solution remains the same, $P_1$. When the liquid–air interface arrives at the boundary, it is pinned by the boundary. When the pressure of the aqueous solution increases, the shape of the interface can be tuned, shown as $\mathrm{I}_\mathrm{B}, \mathrm{II}_1, \mathrm{II}_2, \ldots \mathrm{II}_\mathrm{max}$ in Stage II. The pressure in aqueous solution in Stage II ranges from $P_1$ to $P_\mathrm{max}$. When the pressure increases and exceeds $P_\mathrm{max}$, the liquid–air interface breaks the boundary and flows into the hydrophobic area of the channel. The shape keeps the same, shown as $\mathrm{II}_\mathrm{max}, \mathrm{III}_1, \mathrm{III}_2, \ldots$ in Stage III. The pressure in Stage III maintains at $P_\mathrm{max}$.

where $r$ and $R$ are defined as the radii of curvature in directions vertical and parallel to the liquid stream, and $\gamma_\mathrm{LG}$ is the surface tension. We take the straight-line shape hydrophilic–hydrophobic boundary as an example for channel pressure calculations. The dimension along the boundary is much larger than the channel height. Therefore, the radius parallel to the liquid stream $R$ is $\infty$. Equation (1) is reduced to

$$\Delta P = P - P_0 = \frac{\gamma_\mathrm{LG}}{r}. \tag{2}$$

It can be expressed as

$$r = \frac{h}{2\cos(180^\circ - \theta)} \tag{3}$$

where $h$ is the height of the channel. Thus

$$P - P_0 = \frac{2\gamma_\mathrm{LG}}{h}\cos(180^\circ - \theta). \tag{4}$$

During Stage I, the liquid–air interface forms a meniscus with a fixed contact angle with the top or bottom surface of the channel, $\theta_1$, which is equal to the contact angle formed by a drop of the same aqueous solution on the same glass hydrophilic surface, $\theta_\mathrm{hydrophilic}$ [18]. Therefore, in Stage I, from (3) and (4), the radius of the meniscus at this stage $r_1$ and the channel pressure $P_1$ are fixed value. Because in the hydrophilic side of the channel, $\theta_1 < 90^\circ$, $r_1$ is negative, and $P_1$ is smaller than $P_0$. Note that the aqueous solution is pumped into the H-channel from the hydrophilic side with a syringe pump at a low rate such that the liquid–air interface demonstrates static rather than dynamic behaviors. Therefore, the liquid–air interface moves toward the hydrophilic–hydrophobic boundary with a fixed shape of meniscus.

During Stage II, when the liquid–air interface arrives at the hydrophilic–hydrophobic boundary, the two contact lines of the liquid–air interface with the top and bottom surfaces of the channel are pinned. Keeping introducing the aqueous solution into the hydrophilic side of the channel, the meniscus of the liquid–air interface changes from concave ($r < 0$) to flat ($r = \infty$), and to convex ($r > 0$). The contact angle between the liquid–air interface and the channel surface $\theta$ increases from $\theta_1$ until $\theta_\mathrm{max}$. $\theta_\mathrm{max}$ is the maximum contact angle that can be sustained by the boundary. $\theta_\mathrm{max}$ is equal to the contact angle formed by a drop of the same aqueous solution on the same Au or Cu hydrophobic surface $\theta_\mathrm{hydrophobic}$ [18]. To prove this, energy technique is employed at the critical pressure equilibrium [30]. At equilibrium of the point just before breaking the pinning of the hydrophilic–hydrophobic boundary [31]

$$\gamma_\mathrm{LV}(dA_\mathrm{f} + dA_\mathrm{c}) = dA_\mathrm{f}(\gamma_\mathrm{AuG} + \gamma_\mathrm{LG} - \gamma_\mathrm{AuL}) \tag{5}$$

where $A_\mathrm{f}$ is the area of the flat surface where the aqueous solution makes contact to the top or bottom channel surface, $A_\mathrm{c}$ is the curved area of the aqueous solution (i.e., the liquid–air interface), $\gamma_\mathrm{LG}$ is the aqueous surface tension, $\gamma_\mathrm{AuG}$ is the surface energy of the hydrophobic surface, and $\gamma_\mathrm{AuL}$ is the interfacial energy of the solid surface contacting the aqueous solution. At this time, the contact of the meniscus with the channel top/bottom surface is $\theta_\mathrm{max}$. Geometric analysis shows that

$$\frac{dA_\mathrm{c}}{dA_\mathrm{f}} = \cos\theta_\mathrm{max}. \tag{6}$$

Plugging (6) into (5), we have

$$\gamma_\mathrm{SL} + \gamma_\mathrm{LG}\cos\theta_\mathrm{max} = \gamma_\mathrm{SG} \tag{7}$$

$$\theta_\mathrm{max} = \cos^{-1}\left(\frac{\gamma_\mathrm{SG} - \gamma_\mathrm{SL}}{\gamma_\mathrm{LG}}\right). \tag{8}$$

According to Young's equation

$$\theta_\mathrm{hydrophobic} = \cos^{-1}\left(\frac{\gamma_\mathrm{SG} - \gamma_\mathrm{SL}}{\gamma_\mathrm{LG}}\right) \tag{9}$$

where $\theta_\mathrm{hydrophobic}$ is the contact angle of aqueous solution on the hydrophobic surface.

Therefore, $\theta_\mathrm{max} = \theta_\mathrm{hydrophobic}$.

The pressure in the hydrophilic side of the channel $P$ ranges from $P_1$ to $P_\mathrm{max}$. $P_\mathrm{max}$ is the maximum pressure that can be sustained by the boundary. $P_{\max}$ can be calculated from (4) with $\theta_{\max}$.

During Stage III, when the aqueous solution is further pumped into the channel, the liquid–air interface eventually overcomes the pinning effect of the hydrophilic–hydrophobic boundary and intrudes into the hydrophobic side of the channel. The shape of the meniscus and the channel pressure maintain a fixed value, similar to the situation in Stage I, except that the contact angle $\theta_{\max}$ is larger than 90°, because of the hydrophobicity of the Au or Cu layers. Therefore, $r_3$ is positive and $P_{\max}$ is larger than $P_0$ according to (8) and (9).

Therefore, only in Stage II, the channel pressure and the shape of the liquid–air meniscus can be tuned, while in Stage I and Stage III, channel pressure and interface meniscus are fixed. The contact angle, the radius of curvature of the meniscus, and the channel pressure in these three stages are calculated and plotted in Fig. 7(a). Experimental results of channel pressure are compared with calculations in Fig. 7(a). In this paper, the purpose is to create the liquid–air interface in Stage II without breaking the boundary, and to use the liquid–air interface to conduct interfacial polymerization as described later.

### C. Interfacial Polymerization of the Micropolymer Membrane

After an aqueous solution containing 1,6-diaminohexane is pinned at the liquid–air interface (shown in Fig. 2 as line $\mathrm{AA}'$), an organic solution of adipoyl chloride in toluene is flowed into the channel from the other (hydrophobic) side of the interface. Because of the presence of the aqueous solution and the persistent external pressure from the side of the aqueous solution, the organic solution will not flow across the interface into the hydrophilic side, although the organic solution has good wettability on both glass and SAM-coated Au or Cu surfaces. The aqueous solution and the organic solution precisely contact at the hydrophilic–hydrophobic interface, and reaction takes place between 1,6-diaminohexane and adipoyl chloride to form a nylon membrane. The chemical reaction is described as follows [32], [33]:

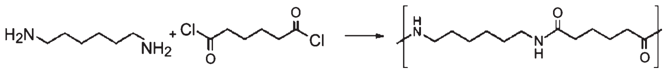

The nylon membrane will precisely follow the 3-D configuration of the liquid–air interface. Using different reagents in the two liquid phases, membranes of different polymer materials can be fabricated accordingly. We fabricate nylon membranes here as a model to demonstrate the method.

## III. Fabrication

Complex Cu patterns on glass with different edge shapes and small feature sizes are achieved by photolithography. To form the microchannel, double-sided adhesive is cut into the shape of the microchannel and is used to bond together the two glass slides with patterned Cu layers.

Microscope glass slides (Fisher Scientific, Pittsburg, PA, USA) are coated with thin layers of titanium/copper/titanium (Ti/Cu/Ti, 225/300/450 Å) using a CVC 601 dc sputterer as shown in Fig. 4(a). The bottom Ti layer (225 Å) is to enhance the adhesion of Cu on the glass substrate and to protect the glass surface from contamination during the fabrication process. The top Ti layer (450 Å) protects the Cu layer from oxidation and from contamination during later process steps.

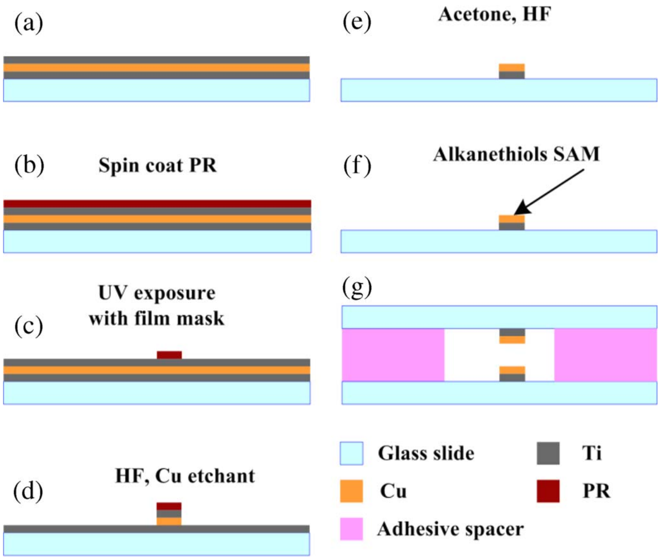

Fig. 4. Process flow of fabricating the device (cross sections; drawing not to scale). (a) Glass slides coated with layers of Ti/Cu/Ti (225/300/450 Å) by sputtering. (b) PR is spin coated on top of the metal layers. (c) PR is patterned by photolithography. (d) Top Ti layer and the Cu layer are etched using HF and Cu etchant, respectively, using PR as the etching mask. (e) PR is removed, and the Ti layer on top of the Cu layer and glass surface is removed with HF. (f) Immersed into the alkanethiols solution, a hydrophobic SAM of alkanethiol molecules forms on top of the Cu layer, and the glass surface remains hydrophilic. (g) Two of the prepared glass slides with treated Cu layers are bonded together with double-sided adhesive.

Positive photoresist (PR) STR-1045 is spin coated on top of the metal layers on the glass slides by a single-wafer spin processor (WS-400E-6NPP-LITE, Laurell Technologies Corporation, PA, USA). To pattern the PR, a printed transparent film is used as the mask, and an ultraviolet lamp (OmniCure Series 2000, EXFO Photonic Solutions, Inc. ON, Canada) is used to expose PR at the intensity of 25 mW/cm$^2$ for 60 s. After patterning PR, Ti etchant (1:10 hydrofluoric (HF) solution) and Cu etchant $[\text{Acetic acid (HAC)} : H_2O_2 : H_2O = 1{:}1{:}10]$ are subsequently used to etch the top protective Ti layer and the Cu layer. The surfaces are rinsed with deionized (DI) water at the end of each step of etching. After the etching, all three metal layers covered by PR are intact, and the bottom adhesion Ti layer in the area without PR protection is exposed, as shown in Fig. 4(d). The masks used in this paper to pattern the metal layers on the glass substrates are shown in Fig. 5. These film masks are printed with the resolution of 3000 dpi by Imagesetter, Inc. (Madison, WI, USA).

Two glass slides coated with the metal layers subjected to the process described above using one of the masks in Fig. 5 are prepared to build the device. Four holes are drilled on one of the slides as the inlets (2, one for hydrophilic/hydrophobic side each) and the outlets (2, one for hydrophilic/hydrophobic side each) of the channels [see Fig. 2(a)]. Next, the exposed Ti (on top of the Cu layer and the glass surface for protection) on both glass slides is finally removed using 1:100 HF solution.

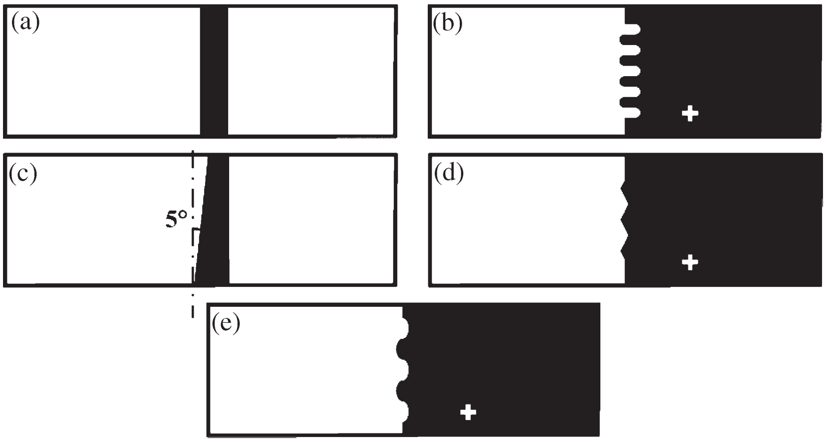

Fig. 5. Film masks for patterning the Cu or Au layers on glass surfaces. (a) For straight-line interface. (b) Interdigital interface. The length of the digit is 4 mm, and its width 2 mm. The radius of curvature at the end of each digit is 2 mm. (c) Twisted interface. Each boundary is rotated by ±5°; therefore, the total twist is 10° between the two boundaries on the top and at the bottom. (d) Zigzag-shaped interface. (e) Wavy interface for the fabrication of a nylon membrane.

The slides with exposed Cu layer and glass surfaces are then immersed into a 1 mM solution of $CH_3(CH_2)_{15}SH$ (Acros Organics, Fair Lawn, NJ, USA) in ethanol for 120 min, followed by rinsing with ethanol for 1 min and drying by nitrogen. A SAM of $CH_3(CH_2)_{15}SH$ is thus formed on the Cu layers, as shown in Fig. 4(f). Commercially available Au-coated glass slides are also used. There is a thin layer of Ti between the Au layer and the glass surface for the purpose of adhesion. The PR patterning process is the same as the one described above. The etchant for Au is GE-8148 (Transene Company, Inc., MA, USA). 250- to 500-$\mu$m-thick double-sided adhesive spacers (3M, St. Paul, MN, USA) are cut into the shape of the channels, as shown in Fig. 2. The glass slides are bonded together using these adhesive spacers; during this bonding step, boundaries between treated metal and glass are aligned or slightly offset or angled to define the potential interfaces. Ethyl vinyl acetate microbore tubings (Cole Parmer Company, IL, USA) are finally plugged into the four inlet/outlet holes on the top glass slide and are sealed by epoxy glue.

## IV. SIMULATION AND EXPERIMENTAL RESULTS

### A. *Contact Angle Measurement*

The contact angles of different fluids on different surfaces used in this paper are tested with a goniometer (OCA-20, DataPhysics Instruments GmbH, Germany). A drop of fluid to be tested is placed on the surface. The image of the profile of the drop on the surface is taken by the goniometer, as shown in Fig. 6. The contact angles are calculated by the accompanying commercial software SCA-20 (DataPhysics Instruments GmbH, Germany) and are listed in Table I.

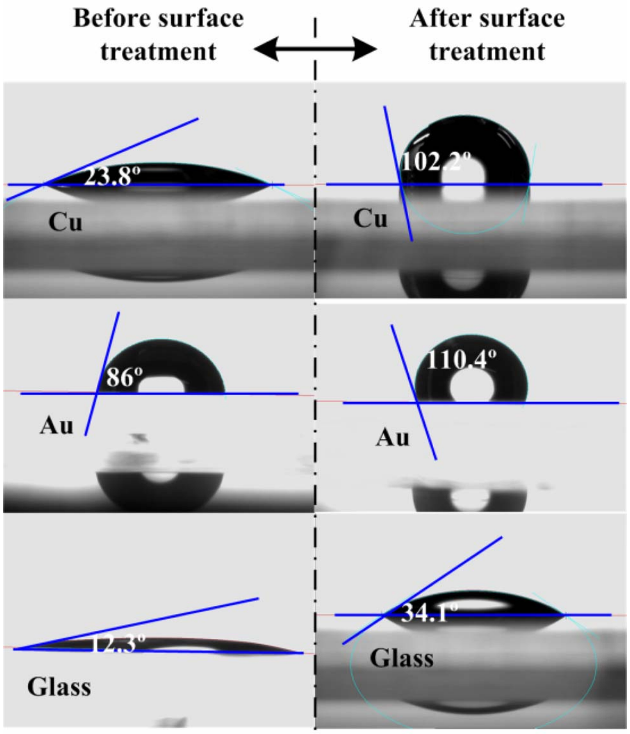

Fig. 6. Images of DI water drops on different surfaces, including Cu, Au, and glass, before and after the surface treatment.

TABLE I
WATER CONTACT ANGLES ON THE SURFACES

| | Before surface treatment [a] | After surface treatment [b] |
|---|---|---|
| Cu | 23.8° | 102.2° |
| Au | 86.0° | 110.4° |
| Glass | 12.3° | 34.1° |

[a] All surface treatments include immersing the surfaces into the 1mM ethanol solution of $CH_3(CH_2)_{15}SH$ for 120 min, followed by ethanol rinsing for 4 min and nitrogen drying.

[b] The Au-coated glass slides are tested as is after they are received from EMF Corporation, Ithaca, NY, USA.

After the surface treatment with alkanethiol solution, Cu or Au surfaces are hydrophobic with contact angles greater than 100°. Glass surfaces remain hydrophilic after the surface treatment. To form the nylon membrane via interfacial polymerization, the aqueous solution (4.76 vol.% of 60% 1,6-diaminohexane in DI water) is flowed into the channel from the hydrophilic side. The contact angles of this aqueous solution on different surfaces are similar to those of DI water. For example, the contact angles of DI water and such aqueous solution on an Au surface after the surface treatment are 110.4° and 104.3°, respectively. The organic solution (3 vol.% adipoyl chloride solution in toluene), which is flowed into the channel from the hydrophobic side, has good wettability on all the surfaces involved in this paper—its contact angle ranges from 10° to 20°.

### B. Simulations

Simulations of the liquid–air interfaces formed at the hydrophilic–hydrophobic boundaries are carried out using Surface Evolver software, a public domain finite element package [34], [35] on a computer with a Core 2 Quad Processor and 2-GB RAM. The Surface Evolver evolves the surface toward minimal energy by a gradient descent method. It has been employed in the studies related to surface tension and multiphase interfaces [36]–[42]. The surface configurations of different interface structures are shown in Figs. 8–10, including the straight-line interface, the curved interface, and the twisted interface. Both the simulated plots and the optical images of the real interfaces are shown and compared. The meshes of the structures are refined three times, and 150 iterations are taken for each surface to evolve. For clearer illustration, the structures are not isometrically depicted as with the real devices.

### C. Imaging and Microscopy

The experiments for creating the liquid–air interfaces and interfacial polymerization of nylon membranes are observed under a stereomicroscope (Nikon SMZ1500, Nikon Instruments, Inc., Melville, NY, USA) connected to a charge-coupled device camera (Imperx Camera, Imperx, Inc., Boca Raton, FL, USA) and interfaced to a computer with SaperaLT CamExpert and StreamPix softwares (DALSA Company, Waterloo, ON, Canada).

### D. Maximum Pressure Sustained by the Hydrophilic–Hydrophobic Interface

Based on the theory described in earlier sections, we first study the maximum pressure in microchannels that the hydrophilic–hydrophobic boundary could sustain. The straight-line hydrophilic–hydrophobic interface formed by the glass-Au boundaries is taken as an example to calculate such maximum pressure. The aqueous solution (4.76 vol.% of 60% 1,6-diaminohexane in DI water) is pumped into the channel from the inlet (shown as (a) in Fig. 2) of the hydrophilic side. When the hydrophilic half of the H-channel (the left side of $\mathrm{BB}'$ in Fig. 2) is filled with the aqueous solution, the outlet (shown as (b) in Fig. 2) of the hydrophilic side is sealed with epoxy glue. At this time, a liquid–air interface is formed in the hydrophilic side of the channel and close to the boundary, as shown in Stage I in Fig. 3. The purpose of sealing the tube (b) is to control the pressure of the liquid in the hydrophilic side by the syringe pump. Otherwise, the open air in the hydrophilic side will make the pressure fixed at a certain value, because of the Young–Laplace relation between the pressure difference at the interface and the contact angle on the channel surface, as discussed above. During the whole process, the inlet (c) and outlet (d) of the hydrophobic side are open to maintain the pressure on the air side of the interface, i.e., the right side in Fig. 3.

The surface tension of the aqueous solution $\gamma_{\mathrm{LG}}$ and its contact angles on hydrophilic and hydrophobic surfaces $\theta_{\mathrm{hydrophilic}}$ and $\theta_{\mathrm{hydrophobic}}$ are tested with the goniometer and are calculated by the software SCA-20. The results are the following: $\gamma_{\mathrm{LG}} = 680.0\ \mu$N/cm, $\theta_{\mathrm{hydrophilic}} = 29.7°$, and $\theta_{\mathrm{hydrophobic}} = 104.3°$. The channel height is obtained by measuring the total thickness of the device $H$ including the thickness of two glass slides (2.000 mm in total) and the height of the channel $h$ by a dial indicator (Mitutoyo, Japan). Then, $h = H - 2.000 = 2.273 - 2.000 = 0.273$ mm.

Therefore, from (4), in Stage I, the channel pressure $P_1$ is 432.725 Pa below $P_0$. In Stage III, the channel pressure in the hydrophilic side of the channel, $P_{\max}$, is calculated to be 123.047 Pa above $P_0$ for the Au-coated glass substrates. In Stage II, the channel pressure $P$ increases from $-432.725$ Pa below $P_0$ to 123.047 Pa above $P_0$. For Cu-coated glass substrates, $P_{\max}$ is calculated to be 105.273 Pa above $P_0$.

When the aqueous solution is being pumped into the hydrophilic side of the channel, the difference between the channel pressure on the hydrophilic side and the atmospheric pressure $\Delta P$ is monitored with a pressure sensor (163PC01D75, Honeywell, Morristown, NJ, USA), as shown in Fig. 2. The output of this pressure sensor is a voltage $V_{\mathrm{out}}$ measured with a multimeter (Test Bench 390A, B&K Precision Corporation, Yorba Linda, CA, USA). The relationship between $V_{\mathrm{out}}$ and $\Delta P$ is given in

$$\Delta P = (V_{\mathrm{out}} - 3.5\ \mathrm{V}) \times 249\ \mathrm{Pa/V} \tag{10}$$

where 3.5 V is the bias voltage corresponding to the atmospheric pressure.

Fig. 7(a) shows measured and calculated $\Delta P$ as time evolves from Stage I through Stage III. In Stage I, the pressure sensor readout is $V_{\mathrm{out},1} = 1.821$ V and stays at a steady level. The channel pressure $P_1$ equals 418.071 Pa below $P_0$. When the aqueous solution arrives at the boundary, i.e., reaching Stage II, the readout starts to increase from $V_{\mathrm{out},1}$ until the aqueous solution breaks into the hydrophobic side of the channel, i.e., Stage III. The maximum pressure recorded in Stage II is at $V_{\mathrm{out,max}} = 3.956$ V. Hence, the maximum pressure that the hydrophilic–hydrophobic interface can sustain, which is the pressure before the system moves from Stage II to Stage III, is 113.544 Pa above $P_0$, consistent with the value calculated using the physical model. Fig. 7(b) shows the image of the interface under the stereomicroscope at the critical point before breaking the boundary. Part of the interface is still visible, appearing as a bright line in the image resulting from the total reflection of the light, while the rest of the interface starts to enter the hydrophobic side, thus becoming invisible.

### E. Liquid–Air Interfaces

The aqueous solution (4.76 vol.% of 60% 1,6-diaminohexane in DI water) is introduced into the inlet of the hydrophilic side of the channel by a syringe pump at the flow rate of 1 $\mu$L/min. The aqueous solution is confined within the hydrophilic side. The 3-D liquid–air interfaces follow and are pinned at the two hydrophilic–hydrophobic boundary lines on the top and bottom surfaces of the microchannels. At the same time, the shapes of the liquid–air interfaces (menisci) also depend on the channel pressure from the hydrophilic side. Photos of the interfaces are

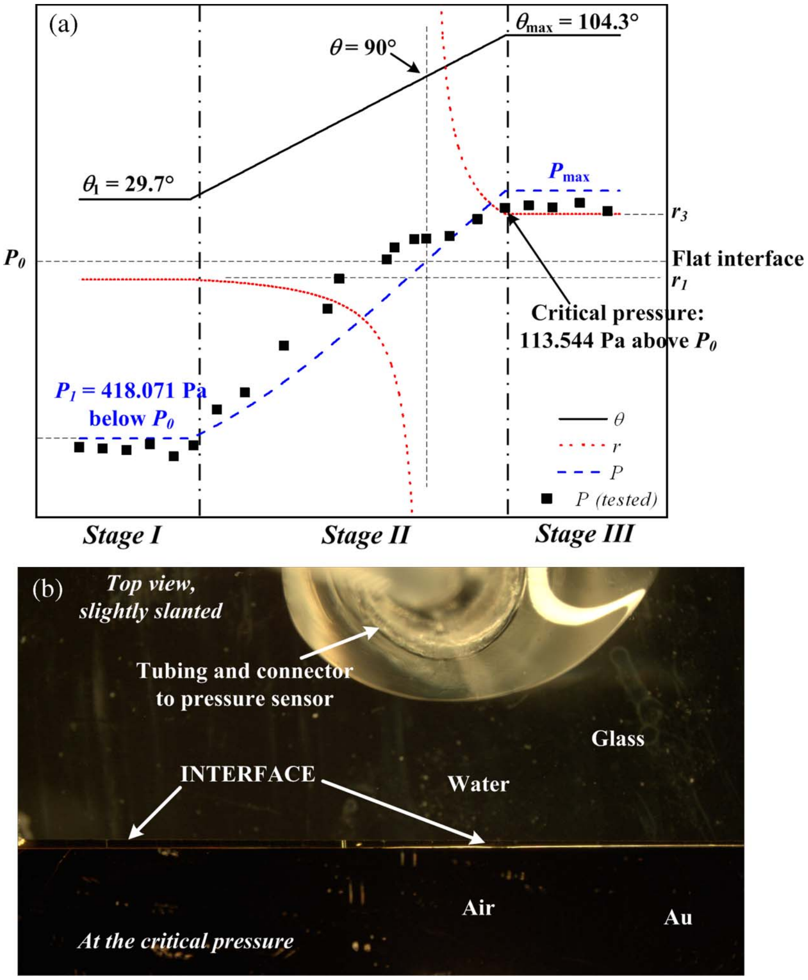

Fig. 7. (a) Qualitative illustration of calculated contact angle $\theta$, the radius of curvature of the meniscus $r$, and the channel pressure $P$, in the three stages, while the aqueous solution is pumped into the channel. $r$ starts as negative in Stage I, becomes $\infty$ (flat interface) at a point in Stage II, and eventually becomes positive in Stage III. Experimentally tested channel pressure in the hydrophilic side is recorded as time evolves, and compared with calculated results. (b) Optical image of the interface at the critical pressure. Part of the liquid–air interface is starting to enter the hydrophobic region, thus becoming invisible.

taken with the stereomicroscope from the top of the devices under the reflective mode. In our experiments, the shape of the liquid–air interface can be precisely controlled, and the fabrication process is highly reproducible $(\text{yield} > 99\%)$.

Because it is hard to directly visualize the geometry of the liquid–air interfaces, they are also studied using Surface Evolver software. The contact angles are input into Surface Evolver; hence, the simulated interfaces always correspond to those at the maximum pressure that can be sustained by the interface.

Fig. 8(d) shows the images of a straight-line liquid–air interface; the simulated interface is shown in Fig. 8(a)–(c). In Fig. 8(a)–(c), the aqueous solution is introduced into the channel from the left side. The top and bottom edges of the interface are formed at the hydrophilic–hydrophobic boundaries, and the interface is a convex meniscus. Note that in Fig. 8(a), the simulation software automatically displays a nonisometric image in order to show the complete structure. The side wall and the top surface on the hydrophobic side (right side) have been set invisible in the simulated images. In the image of the real device [Fig. 8(d)], the bright line is the total reflection image of the liquid–air interface. Under the transmission mode of the stereomicroscope, the thin Cu layers are translucent, and the aqueous solution is observed not to cross the boundary and not to enter the hydrophobic region of the channel, i.e., the region defined between the Cu layers. The straight-line liquid–air interface is 15 mm in length and is robust enough to survive the flipping and shaking during the handling.

In another device, Cu layers are patterned into an interdigital shape, as shown in Fig. 9(d). The fingers are 4 mm in length and 2 mm in width. At the end of each digit, curved liquid–air interface with 1-mm radius of curvature is formed. Fig. 9(a)–(c) shows the simulated structure of one fingertip, which is a curved interface. The aqueous solution is introduced into the channel from the left side. Again, the two curved edges of the interface follow the hydrophilic–hydrophobic boundaries. The interface is a convex meniscus as well. The optical image of the interdigit-shaped device structure [Fig. 9(d)] shows both the top view of the curved interface, and when the device is tilted by 45°. In the geometry of this structure, the liquid–air interface has different maximum pressure in three sites: A, B, and C, as shown in Fig. 9(a). The radius parallel to the liquid stream $R$ [as in (6)] is 1 mm, $\infty$, and $-1$ mm at A, B, and C, respectively. $r = 0.532$ mm, obtained from (8), with $\theta = \theta_{\text{hydrophobic}} = 104.3°$, $h = 0.263$ mm for this device. The maximum pressures that can be sustained by the hydrophilic–hydrophobic boundary

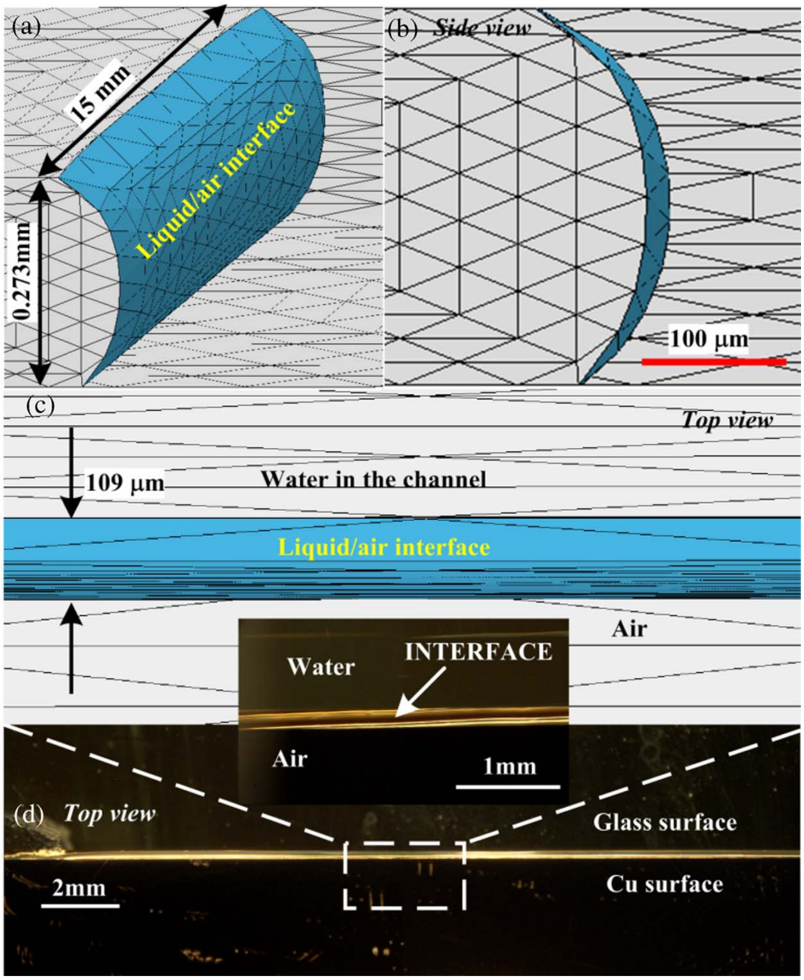

Fig. 8. (a)–(c) Simulated structure of a straight-line liquid–air interface using Surface Evolver. The interface is 15-mm long and 0.273-mm tall. The aqueous solution is introduced from the left. The top hydrophobic surface on the right side of the boundary is set invisible for better illustration of the interface. The shown 3-D view of the simulated interface in (a) is automatically set by Surface Evolver to nonisometric display. The liquid–air interface is pinned at the top and bottom hydrophilic–hydrophobic boundaries, which are defined by different contact angles of the aqueous solution on the surfaces in the simulation program. The simulated interface appears as a straight line from the top view in (c) and a curved meniscus from the side view in (b). In (c), the image is cropped in order to clearly illustrate a part of the interface. In the image of the real straight-line interface taken by a stereomicroscope (d), the aqueous solution is introduced from the hydrophilic side of the channel, i.e., from the top part of the image, and is blocked at the Cu boundaries on the top and bottom surfaces. The bright line in the image is the total reflection of the incident light from the stereomicroscope.

at these three sites are calculated to be: $P_{\max,\mathrm{A}} = 195.820$ Pa, $P_{\max,\mathrm{B}} = 127.820$ Pa, and $P_{\max,\mathrm{C}} = 59.820$ Pa above $P_0$. Therefore, site C, which is a concave boundary, is the most vulnerable point in this system. The maximum pressure that can be sustained by the whole interdigital shape boundary is thus $P_{\max,\mathrm{C}} = 59.820$ Pa above $P_0$.

When two straight-line hydrophilic–hydrophobic boundaries on the top and bottom surfaces are not aligned but are angularly offset, the liquid–air interface is formed as a twisted plane. As shown in the simulated images in Fig. 10(a)–(c), the two edges on the top and bottom surfaces are offset by 10°. The image of the corresponding fabricated device in Fig. 10(d) confirms that the liquid–air interface formed in the channel bears a complex twisted 3-D shape.

A hydrophilic–hydrophobic boundary with a 120° corner is also patterned, and the liquid–air interface is formed at this boundary, as shown in Fig. 11. Due to the surface tension at the liquid–air interface, a curved interface forms to approximate the 120° corner of the patterned metal edge, as shown in Fig. 11(b). Minimum radius of curvature at the corner can be estimated. Take the corner in the dashed box in Fig. 11 as an example. From (4), the liquid pressure at the straight part of the interface, $P_{\max,\mathrm{straight}} = 123.955$ Pa above $P_0$, given $h = 0.271$ mm for this device, and $\theta_{\mathrm{hydrophilic}} = 104.3^\circ$. The liquid pressure at this corner

$$P_{\mathrm{corner}} - P_0 = \gamma_{\mathrm{LG}} \left( \frac{1}{r} + \frac{1}{R_{\mathrm{corner}}} \right). \qquad (11)$$

At the corner, the liquid–air interface is still in the hydrophilic glass side of the channel, as shown in Fig. 11(b). Therefore, from (3), $r = -0.156$ mm, given $\theta_{\mathrm{hydrophilic}} = 29.7^\circ$. At static condition, $P_{\max,\mathrm{straight}} = P_{\mathrm{corner}}$. Therefore, the minimum radius at the corner, $R_{\mathrm{corner}}$ is 0.121 mm.

### *F. Nylon Membrane*

After an aqueous–air interface is formed in the microfluidic channel, the organic solution, 3 vol.% of adipoyl chloride in toluene, is introduced into the channel from the hydrophobic side. The organic solution is injected from a glass syringe

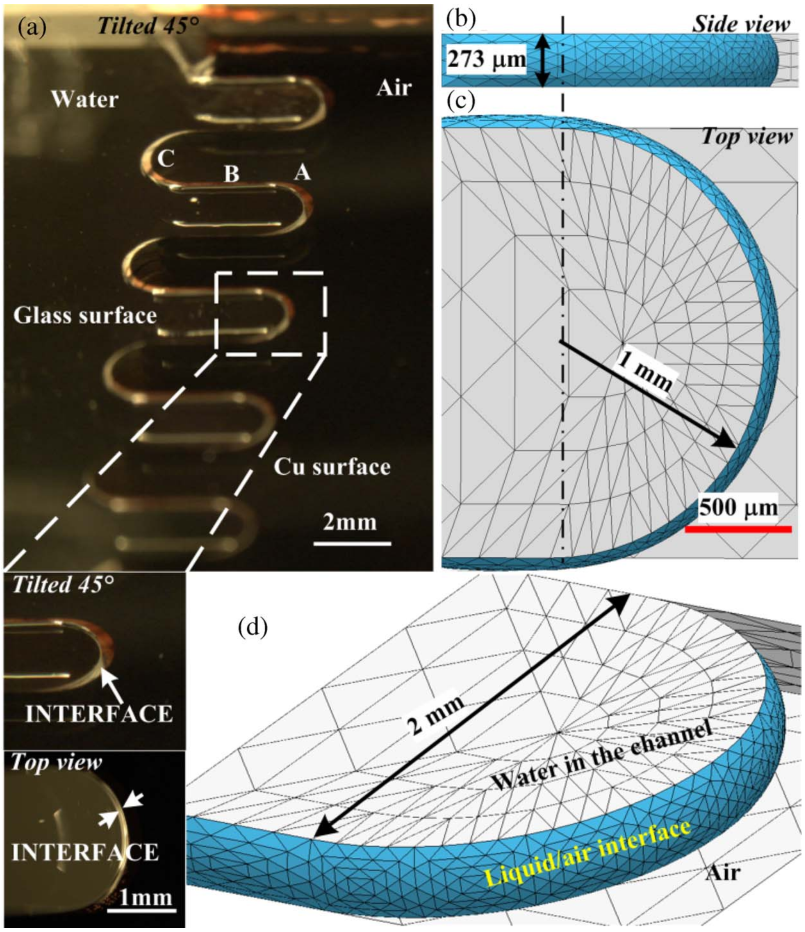

Fig. 9. Interdigitally shaped liquid–air interface. Cu boundaries in an interdigital shape are patterned on two glass surfaces. With two of these boundaries on the top and bottom of the channel aligned to each other, interdigitally shaped liquid–air interface, with curved interface at the end of each digit, is realized. The aqueous solution is introduced into the channel from the hydrophilic side of the channel, i.e., from the left part of the images, and is blocked at the boundaries of the Cu, forming the liquid–air interface following the shape of the boundaries. (a) Optical image of the liquid–air interface taken with a stereomicroscope. (b)–(d) Simulated structure of the curved liquid–air interface. The interface is defined by the curved boundaries of hydrophilic and hydrophobic regions on the top and bottom surfaces.

(Kimble Glass, Inc. and Kontes Glass Company, Vineland, NJ, USA) with a syringe pump. The flow rate is controlled by the syringe pump at 1 $\mu$L/min. The organic solution and the aqueous solution form a liquid–liquid interface with a 3-D shape that is defined by the liquid–air interface. After 15 min of reaction, a nylon membrane that follows the shape of the hydrophilic–hydrophobic boundaries is formed. This membrane is bonded to the surfaces of the channel and is fixed at the former liquid–air interface. To confirm this membrane formation method and examine its robustness, a straight nylon membrane as long as 15 mm and 500 $\mu$m tall is formed in an H-shaped channel (see Fig. 12). Here, the hydrophobic surfaces are chemically treated Cu layers to allow for direct visualization. In the transmission mode of the stereoscope, this nylon membrane is clearly observed, and its thickness is estimated to be 50 $\mu$m obtained from optical images. The aspect ratio (the ratio between the height and the thickness) of the nylon membranes created in the microchannels is thus $10:1$. Another channel with a similar structure but without a membrane is used for comparison. An aqueous food-dye solution is introduced into the channel from the hydrophobic sides of both devices. With the straight-line membrane in the H-shaped channel separating the hydrophobic side of the channel from the hydrophilic side, the food-dye solution is confined within the hydrophobic side, as shown in Fig. 12(a). Without the membrane, the food-dye solution easily crosses the boundaries and flows from the hydrophobic side into the hydrophilic side, as shown in Fig. 12(b).

Glass substrates with patterned Cu layers are further used to fabricate nylon membranes with different shapes. It should be noted that Au-coated glass substrates can be utilized too for this purpose and similar membranes have been formed in our experiments However, the thickness of the Au layer is approximately 1000 Å, making the layer not transparent, thus hard to visualize the formed membranes.

After calculating and testing the maximum pressure that can be sustained by the hydrophilic–hydrophobic boundaries, the pressure of the aqueous solution is controlled by the syringe pump with a flow rate of 1 $\mu$L/min to ensure that the aqueous solution does not cross the hydrophilic–hydrophobic boundaries, and a liquid–air interface is formed. Fig. 13(a) shows a straight-line nylon membrane. Fig. 13(b) shows a nylon membrane inclined 45° to the substrates in a wavy shape. The mask shown in Fig. 5(e) is used to pattern the Cu layer on the substrate. Two of such patterned substrates are aligned so that the wavy boundaries on top and bottom substrates are

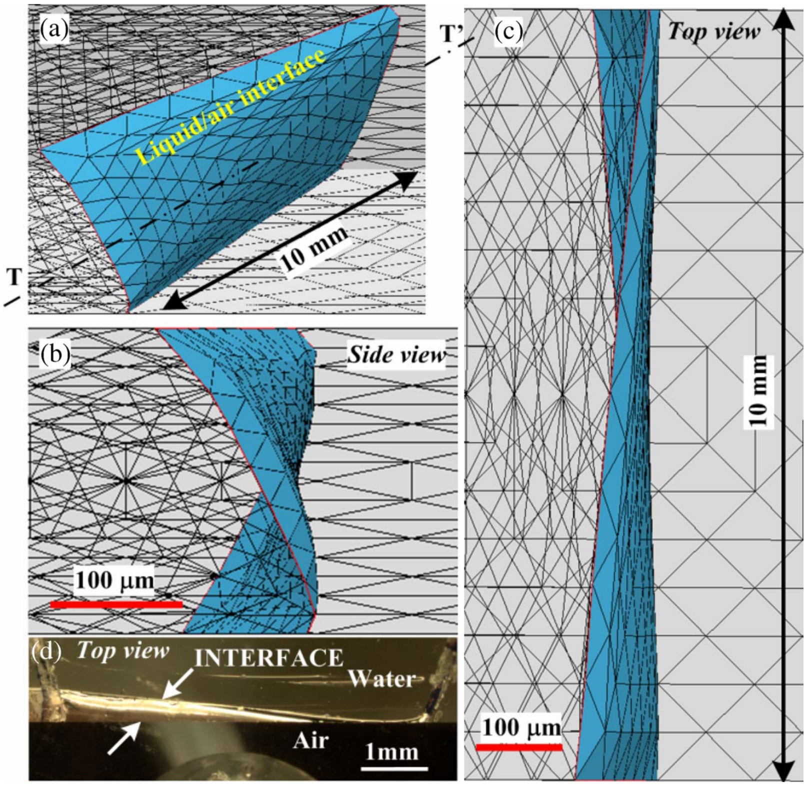

Fig. 10. Hydrophilic–hydrophobic boundaries on the top and bottom of the channel are angularly offset by 10°. (a)–(c) Simulation results show that the liquid–air interface is a plane twisted along TT′. The top surface and the front side wall of the channel are set to be invisible in the simulation program so that the twisted interface can be better illustrated in (b) and (c). In the optical image of the real interface (d), the bright triangular region is part of the twisted interface from the top view.

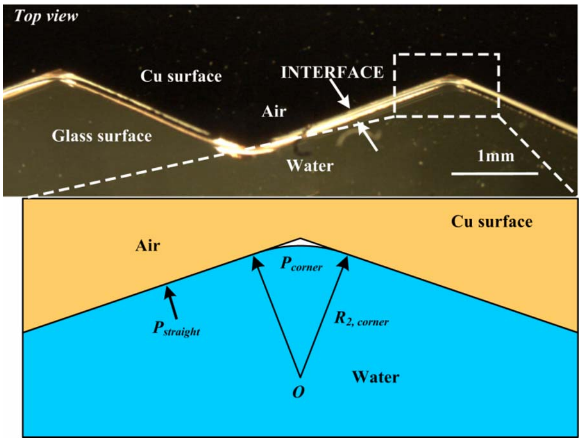

Fig. 11. Zigzagged interface is created at two zigzagged Cu boundaries on the top and bottom surfaces of the microfluidic channel. A curved liquid–air interface is formed at corners of the hydrophilic–hydrophobic boundaries. The inset is the schematic illustration of the interface with a 120° corner in the dashed box.

translationally offset by 270 $\mu$m (equal to the height of the channel) in the direction parallel to the substrate. Therefore, the wavy thin nylon membrane thus formed is inclined with respect to the substrates by 45°. The thin nylon membrane can also be made with a complex 3-D configuration. As an example, a membrane twisted along an axis parallel to the substrate plane (TT′ in Fig. 10) is fabricated by angularly offsetting the two boundary lines by 10°. To make this twisted membrane with a higher aspect ratio, the channel is constructed with the height of 500 $\mu$m, instead of 273 $\mu$m [see Fig. 13(c)].

It should be pointed out that after the membranes are formed at the hydrophilic–hydrophobic boundaries in the microchannels, the aqueous solution can still be introduced from the inlet to the hydrophilic side of the channel through a syringe pump (e.g., at the flow rate of 1 $\mu$L/min). This makes it possible to introduce different aqueous solutions containing different biological or chemical agents to the membrane/interface for potential sensing purpose.

## V. CONCLUSION

We have presented the fabrication of liquid–air and liquid–liquid interfaces with controlled structures and thin nylon membranes with high aspect ratio within microfluidic channels. Hydrophilic–hydrophobic boundaries on channel surfaces have been created by a relatively simple and highly reproducible surface treatment method. The liquid flow can thus be confined within certain areas in the channel without physical channel walls. Taking advantage of these "virtual walls," robust and different liquid–air or liquid–liquid interfaces with complex 3-D structures in microfluidic channels have been realized at the hydrophilic–hydrophobic boundaries. The maximum channel pressure that can be sustained by the boundaries is calculated and experimentally tested. The liquid–air interfaces of different shapes are simulated. Interfacial polymerization is conducted at these interfaces using two immiscible liquid solutions containing the reagents to form nylon membranes with high aspect ratio and controlled structures. The liquid–air interfaces and the polymer membranes formed in the microfluidic channel have

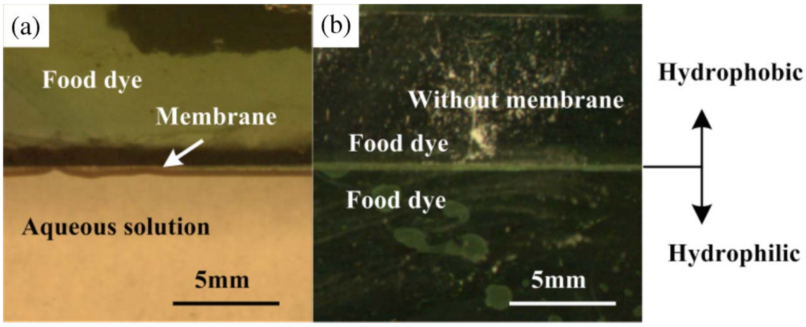

Fig. 12. (a) Green food dye is blocked by a nylon membrane to one side of the interface. The device is placed on top of a piece of white paper to enhance the contrast of display. (b) Without the membrane, the food dye easily crosses the interface.

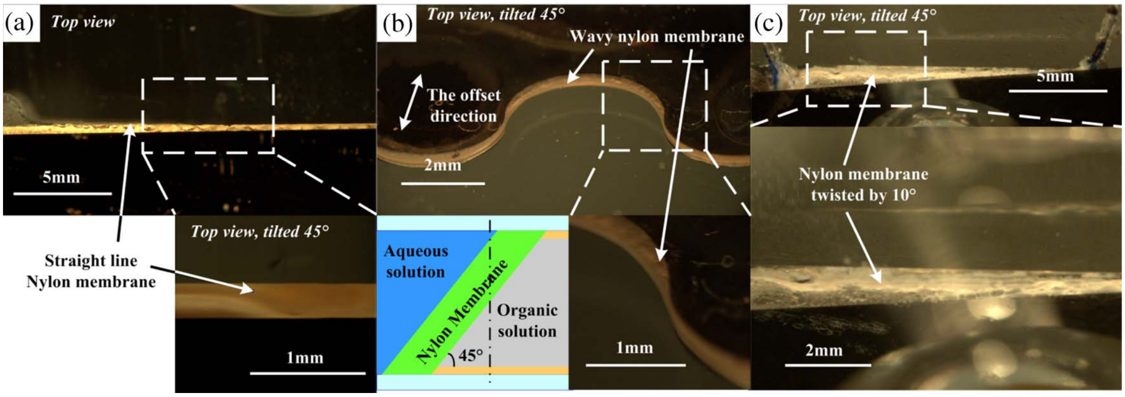

Fig. 13. Different nylon membranes formed within microfluidic channels using pinned liquid–liquid interfaces at the hydrophilic–hydrophobic boundaries. Such boundaries are defined by the patterns of the chemically treated Cu layers. Offsetting the hydrophilic–hydrophobic boundaries on the top and bottom surfaces of the channels can create nylon membranes with different 3-D shapes. The heights of the channels, i.e., the heights of the nylon membranes in the dimension vertical to the substrate, for (a) and (b) are as follows. (a) Nylon membrane formed as a straight line at the hydrophilic–hydrophobic boundaries. The height of the channels in the dimension vertical to the substrates, i.e., the height of the nylon membrane, is 250 $\mu$m. (b) Nylon membrane with a wavy shape. The membrane is slanted against the substrated at 45° because of a 270-$\mu$m translational offset between the top and bottom hydrophilic–hydrophobic boundaries, as shown by the schematic of the cross section. The height of the nylon membrane is also 250 $\mu$m. (c) Nylon membrane with a twisted 3-D structure is formed between two hydrophilic–hydrophobic boundaries on the top and bottom substrates with an angular offset of 10° angle between each other. The height of this channel is 500 $\mu$m in order to obtain a higher aspect ratio of about 10 : 1.

potential applications in microsensing systems. For example, the liquid–air interfaces with different configurations may be used in airborne analytes sensing and detection; the interdigital interfaces can maximize the interfacial area to enhance the sensitivity to the airborne analyte detection. The physical membrane walls can be made of, for instance, peptides that can specifically be dissolved or compromised by target agents for their sensing. These polymer membranes might also find potential applications as sacrificial materials and structures during the fabrication or the operation of microfluidic systems. The mechanism of bonding between the nylon membrane and channel surfaces, more characterization of this nylon membrane, and better imaging of the liquid–air interfaces will be further investigated.

## ACKNOWLEDGMENT

The authors would like to thank Prof. D. J. Beebe and his research group for discussions and access to their facilities. The authors would also like to thank Dr. D. Kim, Dr. S. S. Sridharamurthy, and Dr. L. Dong for the useful discussions and help. H. Jiang would like to thank the 3M Corporation for his Non-Tenured Faculty Award. D. Cheng would like to thank the Materials Science Program, University of Wisconsin—Madison for his Herb Fellowship.

## REFERENCES

[1] B. Zhao, N. O. L. Viernes, J. S. Moore, and D. J. Beebe, "Control and applications of immiscible liquids in microchannels," *J. Amer. Chem. Soc.*, vol. 124, no. 19, pp. 5284–5285, May 15, 2002.

[2] J. Atencia and D. J. Beebe, "Controlled microfluidic interfaces," *Nature*, vol. 437, no. 7059, pp. 648–655, Sep. 29, 2005.

[3] S. S. Sridharamurthy and H. Jiang, "A microfluidic device to acquire gaseous samples via surface tension held gas–liquid interface," *IEEE Sensors J.*, vol. 7, no. 9, pp. 1315–1316, Sep. 2007.

[4] T. Frisk, D. Ronnholm, W. van der Wijngaart, and G. Stemme, "A micromachined interface for airborne sample-to-liquid transfer and its application in a biosensor system," *Lab Chip*, vol. 6, no. 12, pp. 1504–1509, Dec. 2006.

[5] H. Xiao, L. Dong, G. C. Liu, M. Guo, W. L. Xing, and J. Cheng, "Initial study of two-phase laminar flow extraction chip for sample preparation for gas chromatography," *Lab Chip*, vol. 6, no. 8, pp. 1067–1072, Aug. 2006.

[6] N. Srivastava and M. A. Burns, "Microfluidic pressure sensing using trapped air compression," *Lab Chip*, vol. 7, no. 5, pp. 633–637, May 2007.

[7] N. Srivastava and M. A. Burns, "Electronic drop sensing in microfluidic devices: Automated operation of a nanoliter viscometer," *Lab Chip*, vol. 6, no. 6, pp. 744–751, Jun. 2006.

[8] J. D. Salgado, K. Horiuchi, and P. Dutta, "A conductivity-based interface tracking method for microfluidic application," *J. Micromech. Microeng.*, vol. 16, no. 5, pp. 920–928, May 2006.

[9] Y. Y. Luk and N. L. Abbott, "Surface-driven switching of liquid–crystals using redox-active groups on electrodes," *Science*, vol. 301, no. 5633, pp. 623–626, Aug. 1, 2003.

[10] J. M. Brake, M. K. Daschner, Y. Y. Luk, and N. L. Abbott, "Biomolecular interactions at phospholipid-decorated surfaces of liquid crystals," *Science*, vol. 302, no. 5653, pp. 2094–2097, Dec. 19, 2003.

[11] S. S. Sridharamurthy, K. D. Cadwell, N. L. Abbott, and H. Jiang, "A microstructure for the detection of vapor-phase analytes based on orientational transitions of liquid crystals," *Smart Mater. Struct.*, vol. 17, no. 1, art. no. 012 001, Feb. 2008.

[12] S. S. Sridharamurthy, A. K. Agarwal, D. J. Beebe, and H. Jiang, "Dissolvable membranes as sensing elements for microfluidics based biological/chemical sensors," *Lab Chip*, vol. 6, no. 7, pp. 840–842, Jul. 2006.

[13] S. S. Sridharamurthy, L. Dong, and H. Jiang, "A microfluidic chemical/biological sensing system based on membrane dissolution and optical absorption," *Meas. Sci. Technol.*, vol. 18, no. 1, pp. 201–207, Jan. 2007.

[14] B. Zhao, J. S. Moore, and D. J. Beebe, "Surface-directed liquid flow inside microchannels," *Science*, vol. 291, no. 5506, pp. 1023–1026, Feb. 9, 2001.

[15] M. Mrksich and G. M. Whitesides, "Using self-assembled monolayers to understand the interactions of man-made surfaces with proteins and cells," *Annu. Rev. Biophys. Biomol. Struct.*, vol. 25, pp. 55–78, Jun. 1996.

[16] G. M. Whitesides and P. E. Laibinis, "Wet chemical approaches to the characterization of organic-surfaces: Self-assembled monolayers, wetting, and the physical organic-chemistry of the solid liquid interface," *Langmuir*, vol. 6, no. 1, pp. 87–96, Jan. 1990.

[17] G. M. Whitesides, E. Ostuni, S. Takayama, X. Y. Jiang, and D. E. Ingber, "Soft lithography in biology and biochemistry," *Annu. Rev. Biomed. Eng.*, vol. 3, pp. 335–373, 2001.

[18] B. Zhao, J. S. Moore, and D. J. Beebe, "Principles of surface-directed liquid flow in microfluidic channels," *Anal. Chem.*, vol. 74, no. 16, pp. 4259–4268, Aug. 15, 2002.

[19] B. Zhao, J. S. Moore, and D. J. Beebe, "Pressure-sensitive microfluidic gates fabricated by patterning surface free energies inside microchannels," *Langmuir*, vol. 19, no. 5, pp. 1873–1879, Mar. 4, 2003.

[20] A. Hibara, M. Tokeshi, K. Uchiyama, H. Hisamoto, and T. Kitamori, "Integrated multilayer flow system on a microchip," *Anal. Sci.*, vol. 17, no. 1, pp. 89–93, Jan. 2001.

[21] D. Ryan, B. A. Parviz, V. Linder, V. Semetey, S. K. Sia, J. Su, M. Mrksich, and G. M. Whitesides, "Patterning multiple aligned self-assembled monolayers using light," *Langmuir*, vol. 20, no. 21, pp. 9080–9088, Oct. 12, 2004.

[22] A. Hibara, S. Iwayama, S. Matsuoka, M. Ueno, Y. Kikutani, M. Tokeshi, and T. Kitamori, "Surface modification method of microchannels for gas–liquid two-phase flow in microchips," *Anal. Chem.*, vol. 77, no. 3, pp. 943–947, Feb. 1, 2005.

[23] Y. N. Xia, E. Kim, M. Mrksich, and G. M. Whitesides, "Microcontact printing of alkanethiols on copper and its application in microfabrication," *Chem. Mater.*, vol. 8, no. 3, pp. 601–603, Mar. 1996.

[24] E. Hoque, J. A. DeRose, P. Hoffmann, B. Bhushan, and H. J. Mathieu, "Chemical stability of nonwetting, low adhesion self-assembled monolayer films formed by perfluoroalkylsilanization of copper," *J. Chem. Phys.*, vol. 126, no. 11, art. no. 114 706, Mar. 21, 2007.

[25] B. H. Clare and N. L. Abbott, "Orientations of nematic liquid crystals on surfaces presenting controlled densities of peptides: Amplification of protein–peptide binding events," *Langmuir*, vol. 21, no. 14, pp. 6451–6461, Jul. 5, 2005.

[26] D. Cheng, Y. P. Choe, and H. Jiang, "A method to realize controlled air/liquid interfaces and interfacial polymer micro membranes in microfluidic channels," in *Proc. IEEE Sens. Conf.*, Atlanta, GA, 2007, pp. 1044–1047.

[27] P. E. Laibinis and G. M. Whitesides, "Self-assembled monolayers of N-alkanethiolates on copper are barrier films that protect the metal against oxidation by air," *J. Amer. Chem. Soc.*, vol. 114, no. 23, pp. 9022–9028, Nov. 4, 1992.

[28] Y. N. Xia, M. Mrksich, E. Kim, and G. M. Whitesides, "Microcontact printing of octadecylsiloxane on the surface of silicon dioxide and its application in microfabrication," *J. Amer. Chem. Soc.*, vol. 117, no. 37, pp. 9576–9577, Sep. 20, 1995.

[29] E. Ostuni, L. Yan, and G. M. Whitesides, "The interaction of proteins and cells with self-assembled monolayers of alkanethiolates on gold and silver," *Colloids Surf. B, Biointerfaces*, vol. 15, no. 1, pp. 3–30, Aug. 31, 1999.

[30] Y. Y. Feng, Z. Y. Zhou, X. Y. Ye, and H. J. Xiong, "Passive valves based on hydrophobic microfluidics," *Sens. Actuators A, Phys.*, vol. 108, no. 1, pp. 138–143, Nov. 15, 2003.

[31] J. N. Israelachvili, *Intermolecular and Surface Forces*. San Diego, CA: Academic, 1991.

[32] D. Kim and D. J. Beebe, "Porous membrane formation using interfacial fabrication," *J. Appl. Polym. Sci.*, doi: 10.1002/app.27890, to be published.

[33] D. Kim, , "Biological applications of microfluidics using *in situ* fabrication," Ph.D. thesis, Dept. Mech. Eng., Univ. Wisconsin, Madison, WI, 2006.

[34] K. A. Brakke, "The Surface Evolver," *Exp. Math.*, vol. 1, no. 2, pp. 329–338, 1992.

[35] K. A. Brakke, "The Surface Evolver and the stability of liquid surfaces," *Philos. Trans. R. Soc. Lond. Ser. A—Math. Phys. Eng. Sci.*, vol. 354, no. 1715, pp. 2143–2157, Sep. 16, 1996.

[36] J. Silver, Z. H. Mi, K. Takamoto, P. Bungay, J. Brown, and A. Powell, "Controlled formation of low-volume liquid pillars between plates with a lattice of wetting patches by use of a second immiscible fluid," *J. Colloid Interface Sci.*, vol. 219, no. 1, pp. 81–89, Nov. 1, 1999.

[37] F. Wakai, N. Enomoto, and H. Ogawa, "Three-dimensional microstructural evolution in ideal grain growth—General statistics," *Acta Mater.*, vol. 48, no. 6, pp. 1297–1311, Apr. 3, 2000.

[38] Y. W. Chan, T. H. Ju, S. A. Hareb, Y. C. Lee, J. S. Wu, and M. J. Li, "Reliability modeling for ball grid array assembly with a large number of warpage affected solder joints," *J. Electron. Packag.*, vol. 124, no. 3, pp. 246–253, Sep. 2002.

[39] D. C. Whalley and P. P. Conway, "Simulation and interpretation of wetting balance tests using the Surface Evolver," *J. Electron. Packag.*, vol. 118, no. 3, pp. 134–141, Sep. 1996.

[40] W. Lin, S. K. Patra, and Y. C. Lee, "Design of solder joints for self-aligned optoelectronic assemblies," *IEEE Trans. Compon. Packag. Manuf. Technol. B, Adv. Packag.*, vol. 18, no. 3, pp. 543–551, Aug. 1995.

[41] C. Bailey, D. Wheeler, and M. Cross, "An integrated modeling approach to solder joint formation," *IEEE Trans. Compon. Packag. Technol.*, vol. 22, no. 4, pp. 497–502, Dec. 1999.

[42] S. G. Kim, D. I. Kim, W. T. Kim, and Y. B. Park, "Computer simulations of two-dimensional and three-dimensional ideal grain growth," *Phys. Rev. E, Stat. Phys. Plasmas Fluids Relat. Interdiscip. Top.*, vol. 74, no. 6, art. no. 061 605, Dec. 2006.

**Daming Cheng** received the B.S. and M.S. degrees in materials science and engineering from Tsinghua University, Beijing, China, in 2003 and 2005, respectively. He is currently working toward the Ph.D. degree in materials science at the University of Wisconsin—Madison, Madison.

His current research includes the development of multiphase interfaces in microfluidic channels, interfacial polymerization of thin membranes with high aspect ratio, and biological and chemical sensing using liquid crystal.

**Young-Joon Paul Choe** received the B.S. degree in applied mathematics engineering and physics from the University of Wisconsin—Madison, Madison, in 2007. He is currently working toward the M.S. degree in industrial engineering at Northwestern University, Evaston, IL.

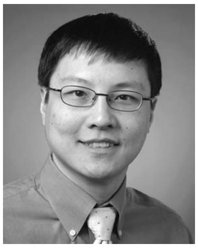

**Hongrui Jiang** (S'98–M'02) received the B.S. degree in physics from Peking University, Beijing, China, and the M.S. and Ph.D. degrees in electrical engineering from Cornell University, Ithaca, NY, in 1999 and 2001, respectively.

He is currently an Assistant Professor with the Department of Electrical and Computer Engineering, a Faculty Affiliate with the Department of Biomedical Engineering, and a Faculty Member of the Materials Science Program, University of Wisconsin (UW)—Madison, Madison. Before he joined the faculty at UW, he was a Postdoctoral Researcher with the Berkeley Sensor and Actuator Center, University of California—Berkeley, Berkeley, from 2001 to 2002. His research interests are in microfabrication technology, biological and chemical microsensors, microactuators, optical MEMS, smart materials and micro/nanostructures, lab on a chip, and biomimetics and bioinspiration.

Dr. Jiang received the National Science Foundation CAREER Award and the Defense Advanced Research Projects Agency Young Faculty Award in 2008.